

Materials Advances

Accepted Manuscript

This article can be cited before page numbers have been issued, to do this please use: U. Pak, D. Che Gal, S. Jang and U. Jong, *Mater. Adv.*, 2025, DOI: 10.1039/D5MA01099C.



This is an Accepted Manuscript, which has been through the Royal Society of Chemistry peer review process and has been accepted for publication.

Accepted Manuscripts are published online shortly after acceptance, before technical editing, formatting and proof reading. Using this free service, authors can make their results available to the community, in citable form, before we publish the edited article. We will replace this Accepted Manuscript with the edited and formatted Advance Article as soon as it is available.

You can find more information about Accepted Manuscripts in the [Information for Authors](#).

Please note that technical editing may introduce minor changes to the text and/or graphics, which may alter content. The journal's standard [Terms & Conditions](#) and the [Ethical guidelines](#) still apply. In no event shall the Royal Society of Chemistry be held responsible for any errors or omissions in this Accepted Manuscript or any consequences arising from the use of any information it contains.

Journal Name

ARTICLE TYPE

Cite this: DOI: 10.1039/xxxxxxxxxx

Theoretical insights into lattice dynamics and thermal transport properties of lead-free quadruple halide perovskite $\text{Cs}_4\text{CuSb}_2\text{Cl}_{12}$ [†]

Un-Sok Pak,* Dok-Song Che Gal, Song-Myong Jang and Un-Gi Jong*

Received Date

Accepted Date

DOI: 10.1039/xxxxxxxxxx

www.rsc.org/journalname

In spite of extensive studies of halide perovskites, little attention has been paid to lattice dynamics and thermal transport properties of halide perovskite $\text{Cs}_4\text{CuSb}_2\text{Cl}_{12}$ so far. In this work, we systematically investigate structural, mechanical, lattice dynamics and thermal transport properties for lead-free quadruple halide perovskite $\text{Cs}_4\text{CuSb}_2\text{Cl}_{12}$ in monoclinic phase using state-of-the-art first-principles methods. Scrutiny of crystal structure reveals that Cs atoms are located inside over-sized cage-like structure CsCl_{12} , while Cu (Sb) atoms are tightly filled into octahedral $\text{Cu}(\text{Sb})\text{Cl}_6$, expecting a role of atomic rattler for the Cs atoms. We carry out anharmonic lattice dynamics calculations at finite temperature based on self-consistent phonon theory, finding that monoclinic $\text{Cs}_4\text{CuSb}_2\text{Cl}_{12}$ is dynamically stable at elevated temperature. Moreover, we find that the Cs atomic rattlers result in lattice anharmonicity and severely scatter heat-carrying acoustic and low-energy optical phonons, consequently leading to low phonon group velocity and extremely short phonon lifetime. We then calculate temperature-dependent lattice thermal conductivity κ_l of monoclinic $\text{Cs}_4\text{CuSb}_2\text{Cl}_{12}$ using unified theory of thermal transport for both crystals and glasses, demonstrating an extremely low κ_l of 0.27, 0.36 and 0.14 W/m·K at 300 K along x -, y - and z -axis. Moreover, it is found that nano-structuring can further suppress the κ_l by half. Strong lattice anharmonicity is again confirmed from Grüneisen parameter calculation and temperature dependence of $\kappa_l \propto T^{-0.72}$. In addition, elastic constant calculation demonstrates that monoclinic $\text{Cs}_4\text{CuSb}_2\text{Cl}_{12}$ is mechanically stable with a brittle nature. Our work highlights theoretical insights into lattice dynamics and thermal transport properties of monoclinic $\text{Cs}_4\text{CuSb}_2\text{Cl}_{12}$.

1 Introduction

Lead-based simple perovskite halides APbX_3 (A=Cs, CH_3NH_3 ; X=I, Br, Cl) have been studied extensively for light-absorber application in solar cells¹, X-ray detector² and light-emitting diodes^{3,4}. Most prominently, the perovskite solar cells have reached power conversion efficiencies of up to 25.2%⁵ in only ten years. Computational investigations^{6–8} have demonstrated that the superior optoelectronic properties of APbX_3 are mostly

ascribed to unique electronic configuration of Pb $6s^26p^0$, high crystalline symmetry and high dimensionality of electronic properties. However, the toxicity of lead and poor stability under ambient environmental conditions are the major drawbacks which hinders them from large-scale applications. This leads to great interest in lead-free perovskite exploration^{9–11}.

In this regard, the substitution of Pb with the same group elements of Sn or Ge can maintain the perovskite structure and advanced optoelectronic properties^{12–15}, but unfortunately, this causes more serious stability issues^{16–19} owing to the easy oxidation of Sn^{2+} (Ge^{2+}) to Sn^{4+} (Ge^{4+}), which destroys both the high structural symmetry and electronic configuration of Sn $5s^25p^0$ ($\text{Ge} 4s^24p^0$). Replacing Pb with heterovalent elements such as Bi and Sb results in $\text{A}_3\text{B}_2\text{X}_9$ compounds with improved phase stability. However, their optoelectronic properties become worse compared to them of APbX_3 due to their unfavorable low dimensionality of crystal and electronic structures^{20–23}. In order to maintain the high dimensionality of crystal structure, double halide perovskite $\text{A}_2\text{B}^{\text{I}}\text{B}^{\text{III}}\text{X}_6$ was derived by substituting two Pb^{2+} cations in APbX_3 with B^{I} and B^{III} cations^{24–27}. Although

Metallic Material Institute, Faculty of Materials Science and Technology, Kim Chaek University of Technology, Pyongyang, PO Box 76, Democratic People's Republic of Korea.
 E-mail: pus93916@star-co.net.kp (Un-Sok Pak)
 E-mail: ug.jong@ryongnamsan.edu.kp (Un-Gi Jong)

† Electronic Supplementary Information (ESI) available: Convergence tests of phonon dispersion curve according to the supercell size, comparison of the atomic forces obtained from the density functional theory and compressive sensing lattice dynamics calculations, convergence tests of lattice thermal conductivity according to the size of q -point mesh, heat capacity as a function of temperature, average phonon lifetime and group velocity and self-consistent phonon dispersion curves at different temperatures for the monoclinic $\text{Cs}_4\text{CuSb}_2\text{Cl}_{12}$. See DOI: 10.1039/b000000x/



great freedom of combination between B^I and B^{III} cations provides over 200 double perovskite halides with various chemical and physical properties, they cannot support efficient solar cells because of their unfavorable bandgap and likely formation of cation-cation antisite^{28–31}. A new 3D perovskite-type compound $A_4\bigcirc C^{II}B^{III}X_{12}$ ^{32–39} (\bigcirc =vacancy) was designed by substituting two B^I cations in $A_2B^IB^{III}X_6$ by \bigcirc and C^{II} cation for providing an alternative platform of designing solar cell materials. Lin *et al.*³² synthesized quadruple perovskites $Cs_4CdSb_2Cl_{12}$ and $Cs_4CdBi_2Cl_{12}$ by a solvothermal method and observed steady-state photoluminescence of showing warm orange emission. The quadruple perovskite $Cs_4CuSb_2Cl_{12}$ ³⁶ was fabricated by using a top-down ultrasonic exfoliation technique with a direct bandgap of 1.6 eV and superior optoelectronic properties due to a reduced electron effective mass. Cai *et al.*³⁹ reported the first colloidal fabrication of $Cs_4CuSb_2Cl_{12}$ perovskite-type nanocrystals with a direct bandgap of 1.79 eV, an ultrafast photo-response and narrow bandwidth. On the other hand, Nag's group³⁷ mechanochemically synthesized the $Cs_4CuSb_2Cl_{12}$, demonstrating the magnetic response of Cu^{2+} cation which controls the electronic properties, its thermal and chemical stabilities. Moreover, Karmaker and co-workers⁴⁰ recently predicted a high power conversion efficiency of 23.1% and an open-circuit voltage of 1.2 V in the $Cs_4CuSb_2Cl_{12}$ -based solar cell by computationally optimizing perovskite layer thickness, doping level, defect density and so on.

To the best of our literature search, most investigations mainly concentrated on synthesis methods and optoelectronic properties for the quadruple perovskite halide $Cs_4CuSb_2Cl_{12}$, and thus its mechanical, lattice dynamics and transport properties have never been explored so far. Recently, Delaire *et al.* investigated the structural instability, optical and thermal properties of the lead halide perovskite $CsPbBr_3$, linking soft anharmonic lattice dynamics and optoelectronic properties⁴¹. Moreover, Gupta and co-workers⁴² performed *ab initio* molecular dynamics simulations combined with neutron scattering measurements in the superionic argyrodite Cu_7PSe_6 , highlighting the importance of strongly anharmonic effects on ionic and thermal transport properties of the superionic systems. In this work, we report a systematic investigation of the lattice dynamics and transport properties including phonon dispersion curves, phonon density of states and lattice thermal conductivity for all-inorganic lead-free quadruple halide perovskite $Cs_4CuSb_2Cl_{12}$ using the state-of-the-art first-principles approaches and methods.

2 Computational methods

All the density functional theory (DFT) calculations were performed using the Vienna *ab initio* Simulation Package (VASP)^{43,44}, employing the projector augmented wave (PAW) potentials^{45,46} with the valence electron configurations of $Cs-5s^25p^66s^1$, $Cu-3d^{10}4p^1$, $Sb-5s^25p^3$ and $Cl-3s^23p^5$. We utilized the PBEsol functional⁴⁷ known to accurately predict the lattice constants of all-inorganic halide perovskites^{48–50}, being crucial for a reliable description of lattice dynamics properties. We used a kinetic energy cutoff of 600 eV for a plane-wave basis set and a k -point mesh of $10 \times 10 \times 6$ for Brillouin zone (BZ) integrations, which were enough to guarantee a total energy accuracy as 3.5

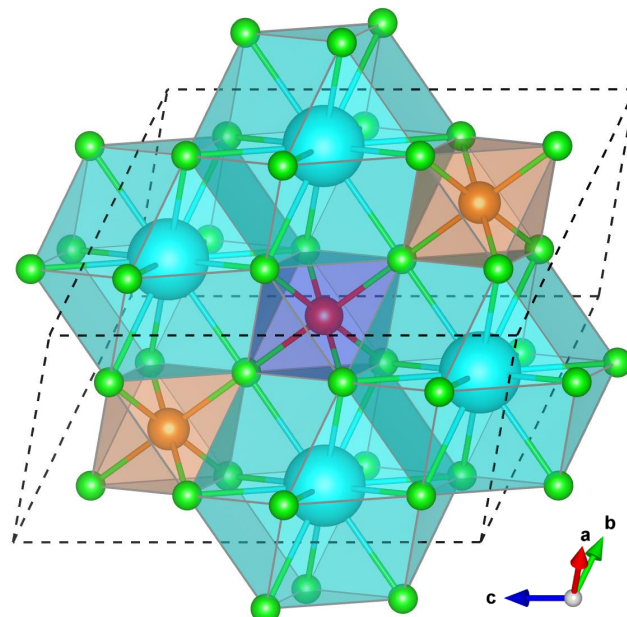


Fig. 1 Polyhedral view for crystalline structure of all-inorganic lead-free quadruple halide perovskite $Cs_4CuSb_2Cl_{12}$ with monoclinic phase of $C2/m$ space group. The cyan, red, orange and green balls represent the Cs, Cu, Sb and Cl atoms, respectively.

meV per atom. Lattice dynamics and thermal conductivity calculations were performed using the ALAMODE code^{51,52}. The atomic positions were relaxed until the atomic forces are smaller than 5×10^{-3} eV/Å, while the energy convergence criterion was set to be 10^{-7} eV. The interatomic force constants (IFCs) were calculated using a $2 \times 2 \times 2$ supercell expansion, and for supercell calculations, we used the same convergence thresholds with a reduced kinetic energy cutoff of 400 eV and $5 \times 5 \times 3$ k -point mesh. In this work, we mainly focused on lattice dynamics and thermal transport properties of $Cs_4CuSb_2Cl_{12}$, and therefore, spin-polarization of Cu^{2+} atoms was not considered.

In order to calculate the harmonic phonon dispersion curves and phonon density of states (DOS), we used the second-order (harmonic) IFCs by utilizing the finite displacement method with $2 \times 2 \times 2$ supercell, as implemented in the ALAMODE code^{51,52}. We prepared 20 different supercells where all the atoms were randomly displaced by 0.01 Å from their equilibrium positions, and then, calculated the atomic forces for each displaced configurations, extracting harmonic IFCs by using the ALAMODE code. We performed the convergence tests of the phonon eigenvalues with respect to the supercell size, revealing that the results of $2 \times 2 \times 2$ supercell agree well with the ones of $3 \times 3 \times 3$ supercell for $Cs_4CuSb_2Cl_{12}$ as shown in Fig. S1, ESI†. We performed the self-consistent phonon (SCP) calculations in order to include the anharmonic effects at finite temperatures^{51–53}. Within the SCP theory, the anharmonic phonon eigenvalues were computed as functions of temperature from the pole of the Green's function beyond the perturbation theory, as implemented in the ALAMODE code. In the SCP equation, the phonon self-energy becomes frequency-dependent only treating the loop diagram related with the quartic IFCs. Note that the off-diagonal elements of the self-



energy should be accounted to allow the phonon eigenvectors to change by anharmonic effects⁵². The current SCP approach applied to this work was confirmed to be efficient and accurate in accounting for lattice dynamics and thermal transport properties of systems with severe anharmonicity. For estimating anharmonic IFCs, we employed the compressive sensing lattice dynamics (CSLD) approach⁵⁴, as implemented in the ALAMODE code. To do this, we prepared over 60 configurations where all of the atoms are displaced randomly with large displacements⁵⁴ and computed atomic forces for each configuration using precise DFT calculations. For cubic and quartic IFCs, we included up to 5th- and 3rd-nearest neighbor shells, whereas fifth- and sixth-order IFCs were considered for nearest-neighbor pairs. In order to estimate the accuracy of the IFCs estimated by the CSLD, we show the comparison of the atomic forces obtained from DFT and CSLD calculations in Fig. S2, ESI†. By using the higher-order IFCs, we guaranteed a relative error below 2.6 % for the fitting of the atomic forces compared with the DFT-calculated forces.

With the calculated 3rd-order IFCs, we solved the Boltzmann transport equation (BTE) for phonon within the relaxation time approximation (RTA) and estimated the lattice thermal conductivity, as implemented in the ALAMODE code. We performed convergence test for the calculations of lattice thermal conductivity κ_l according to the size of q -point mesh in the phonon BZ, demonstrating that a $20 \times 20 \times 15$ q -point mesh is sufficient to determine κ_l with an error less than 0.01 W/m·K (see Fig. S3, ESI†). On the other hand, it was recently suggested that both diagonal and off-diagonal contributions to κ_l can be calculated from the phonon velocity operator based on the unified theory of thermal transport for both crystals and glasses⁵⁵. Furthermore, it was demonstrated that the off-diagonal contributions were found to be essential even after the anharmonic phonon renormalization was taken into account in recent studies^{56–58} on the lattice thermal conductivity. By solving the Boltzmann transport equation (BTE) on top of the SCP phonon dispersions, the Peierls's contribution κ_{lP} to the lattice thermal conductivity κ_l was estimated from the harmonic and cubic IFCs, as implemented in the ALAMODE code. Meanwhile, the coherent contribution κ_{lC} was calculated using the phonon velocity operator within the framework of unified theory for the lattice transport properties⁵⁵, as implemented in ALAMODE code.

The mechanical stability of materials with polycrystalline structure can be determined by elastic constants including bulk (B), shear (G) and Young's (E) moduli. Such elastic moduli were estimated from the elastic stiffness (C_{ij}) and compliance (S_{ij}) constants for the single crystal material, which were obtained from the density functional perturbation theory (DFPT) calculations⁵⁹. For a monoclinic structure, the mechanical stability criterion can

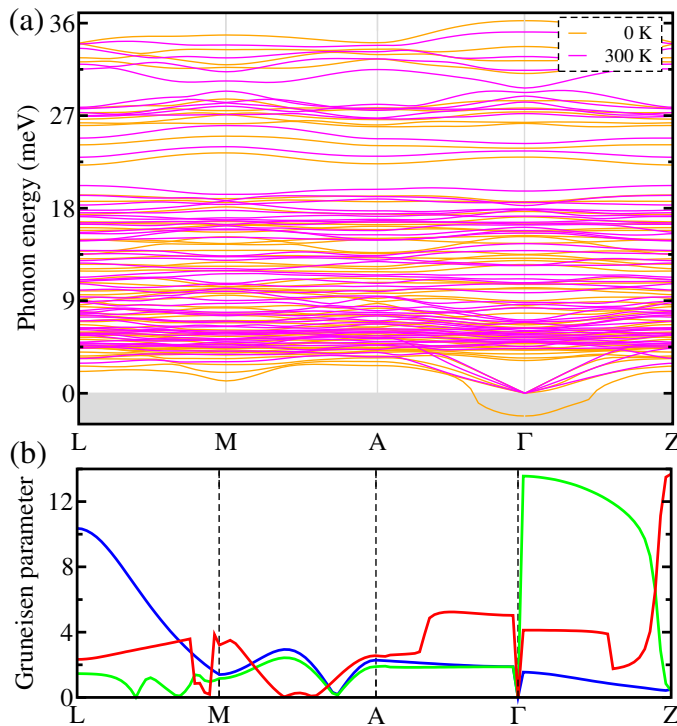


Fig. 2 (a) Phonon dispersion curves calculated at 0 K (brown) and 300 K (magenta) by utilizing self-consistent phonon (SCP) theory and (b) Grüneisen parameter corresponding to longitudinal (red) and two transverse acoustic phonon modes (green and blue) for quadruple halide perovskite $\text{Cs}_4\text{CuSb}_2\text{Cl}_{12}$ with monoclinic phase of $\text{C}2/\text{m}$ space group.

be expressed as follows.

$$C_{11} > 0, C_{22} > 0, C_{33} > 0, C_{44} > 0, C_{55} > 0, C_{66} > 0 \quad (1)$$

$$C_{11} + C_{22} + C_{33} + 2(C_{12} + C_{13} + C_{23}) > 0 \quad (2)$$

$$C_{33}C_{55} - C_{35}^2 > 0, C_{44}C_{66} - C_{46}^2 > 0, C_{22}C_{33} - 2C_{23} > 0 \quad (3)$$

$$C_{22}(C_{33}C_{55} - C_{35}^2) + 2C_{23}C_{25}C_{35} - C_{23}^2C_{55} - C_{25}^2C_{33} > 0 \quad (4)$$

The elastic moduli B, G and E are important factors for describing the materials resistance against the mechanical deformation. Moreover, the Pugh criteria⁶⁰ implies that polycrystalline materials with the Pugh's ratio B/G and the Poisson's ratio $\nu = \frac{3B - 2G}{2(3B + G)}$ smaller (larger) than 1.75 and 0.26, respectively are regarded as brittle (ductile) materials.

3 Results and discussion

3.1 Structural properties

We begin with scrutinizing the crystalline structure of the quadruple halide perovskite $\text{Cs}_4\text{CuSb}_2\text{Cl}_{12}$. According to the previous experiment³⁹, $\text{Cs}_4\text{CuSb}_2\text{Cl}_{12}$ crystallizes in the monoclinic phase with the $\text{C}2/\text{m}$ space group. By performing the variable-cell structural optimization, we obtained the PBEsol-optimized lattice constants of $a=13.12$ Å, $b=7.36$ Å, $c=13.02$ Å and $\beta=112.59^\circ$ in good agreement with the previous experimental results³⁹ of $a=13.04$ Å, $b=7.30$ Å, $c=12.97$ Å and $\beta=111.73^\circ$. Fig. 1 dis-

plays the polyhedral view of the PBEsol-optimized crystal structure for the quadruple halide perovskite $\text{Cs}_4\text{CuSb}_2\text{Cl}_{12}$ with the monoclinic $C2/m$ space group. A particular structural feature is that its crystalline structure consists of corner- and face-sharing cage-like structures composed of Cl^- anions, which accommodate one metal cation among Cs^+ , Cu^{2+} and Sb^{3+} . That is, the Cu^{2+} (Sb^{3+}) cations are at the center of CuCl_6 (SbCl_6) octahedral cages, while the Cs^+ cations are located inside the cub-octahedral cages. Moreover, the average value of $\text{Cu}-\text{Cl}$ ($\text{Sb}-\text{Cl}$) bond length was measured to be 2.47 (2.61) Å which is slightly smaller (larger) than the sum of ionic radii of 2.54 (2.57) Å for Cu^{2+} (Sb^{3+}) and Cl^- ions. However, the average distance 3.69 Å between the Cs^+ cation and the Cl^- anion is much greater compared to the sum of ionic radii of 3.48 Å for the corresponding ions. This obviously indicates that the Cs atoms are located inside the oversized cub-octahedral CsCl_{12} cages, whereas the Cu and Sb atoms are tightly filled into the octahedral CuCl_6 and SbCl_6 cages, respectively. From such structural feature of $\text{Cs}_4\text{CuSb}_2\text{Cl}_{12}$, it can be expected that the Cs atoms play roles as the vibrational rattlers because of fairly large interstitial space in the CsCl_{12} cub-octahedral cage, driving the lattice anharmonicity like A atoms in the halide perovskites ABX_3 .^{61,62}

3.2 Mechanical and elastic properties

Solar cell materials are utilized to directly generate electricity by absorbing sunlight for the application of the solar cell system. For that reason, their mechanical property is an important factor as it determines solar cell system's safety and durability under operation. Within the DFPT approach, we estimated the independent elastic stiffness constants of C_{11} , C_{22} , C_{33} , C_{44} , C_{55} , C_{66} , C_{12} , C_{13} , C_{23} , C_{25} , C_{35} and C_{46} to be 16.49, 20.97, 18.39, 5.62, 5.60, 6.50, 6.65, 5.94, 6.47, 0.99, 2.02 and 0.22 GPa, respectively for the monoclinic $\text{Cs}_4\text{CuSb}_2\text{Cl}_{12}$. We found that these elastic stiffness constants satisfy the Born's stability criteria for the monoclinic solid crystals, expressed by the eqn. 1–4, thus indicating the mechanical stability at ambient condition. It should be noted that the deformation resistance and mechanical stability along the x -, y - and z -axis are superior than the shear deformation resistance and stability because the C_{ii} ($i=1,2,3$) is larger by one order in magnitude than the C_{ij} ($i\neq j$). Meanwhile, we obtained $B = 10.44$ GPa, $E = 15.10$ GPa and $G = 6.00$ GPa for the polycrystalline $\text{Cs}_4\text{CuSb}_2\text{Cl}_{12}$, implying that uniform pressure and uniaxial stress are larger than the shear stress owing to the larger value of B and E than the value of G . It was found that the monoclinic $\text{Cs}_4\text{CuSb}_2\text{Cl}_{12}$ is considered as a brittle material because of its Poisson's ratio ν of 0.26 and Pugh's ratio B/G of 1.74 being smaller than the threshold values of 0.26 and 1.75. For describing the elastic anisotropy, we obtained the universal anisotropic index $A^U = 0.29$, finding the much deviation from zero, *i.e.*, from the isotropic nature. Furthermore, we determined the relatively low average sound velocity and Debye temperature of 1469.98 m/s and 136.60 K by using the calculated elastic moduli.

3.3 Lattice dynamics properties

At the next step, we carried out lattice dynamics calculations for the monoclinic $\text{Cs}_4\text{CuSb}_2\text{Cl}_{12}$ using $2\times 2\times 2$ supercells in order to investigate its dynamical stability, phonon energies and density of state (DOS). Dynamical stability and thermal vibration of constituent atoms at a given temperature are determined by lattice dynamics for crystalline solids. Fig. 2(a) shows the harmonic phonon dispersion curves (brown) calculated at 0 K along the L–M–A–Γ–Z line of the phonon Brillouin zone (BZ). As can be seen, the soft phonon modes with imaginary phonon energies were identified at the Γ point for the monoclinic $\text{Cs}_4\text{CuSb}_2\text{Cl}_{12}$. This fact seems to be at odds with the experimental finding that $\text{Cs}_4\text{CuSb}_2\text{Cl}_{12}$ adopts the monoclinic phase at ambient condition^{38,39}. However, Xie and co-workers⁶² already found that the anharmonic soft modes could be shown even for the dynamically stable cubic CsSnI_3 , which was associated with the strong lattice vibrations of atomic rattlers, resulting in the octahedral distortions of SnI_6 . Actually, we observed the $\text{Cu}(\text{Sb})\text{Cl}_6$ octahedral and CsCl_{12} cub-octahedral distortions with the elongation along the z direction and shortening in the x - y plane for the metal-chlorine bond lengths, being ascribed to the Jahn-Teller effect owing to the presence of metal cations with the unpaired electrons as confirmed in the previous experiment³⁹. Namely, it is expected that the anharmonic phonon modes are just induced by the rattling vibrations of the metal cations, especially by the Cs-atomic rattling vibrations.

In order to directly measure the lattice anharmonicity, we also computed the Grüneisen parameter associated with the acoustic phonon modes for the monoclinic $\text{Cs}_4\text{CuSb}_2\text{Cl}_{12}$ as implemented in the ALAMODE code^{51,52}. In general, the Grüneisen parameters are determined by the change of phonon energies according to the volume of the unit cell⁶³. As can be seen in Fig. 2(b), the Grüneisen parameters reached the maximum value over 12 in the Γ –Z line of the phonon BZ with an average value of 3.9. Such a large Grüneisen parameter is comparable for the one of 4.1 for the strongly anharmonic SnSe ⁶⁴, suggesting strong lattice anharmonicity and thus low lattice thermal conductivity for $\text{Cs}_4\text{CuSb}_2\text{Cl}_{12}$. On the other hand, we calculated the atom-resolved phonon density of states (DOS) of the monoclinic $\text{Cs}_4\text{CuSb}_2\text{Cl}_{12}$ at 0 K. As shown in Fig. 3(a), the phonon DOS calculation revealed that the soft phonon modes are dominantly originated from the Cs and Cl atoms with a small contribution of Cu and Sb atoms. The Cs atoms make a major contribution to the acoustic and low-energy optical phonon modes, whereas the Cl to the mid- and high-energy optical modes. From the presence of such soft modes, it can be regarded that at 0 K, the quadruple halide perovskite $\text{Cs}_4\text{CuSb}_2\text{Cl}_{12}$ is dynamically unstable in the monoclinic phase. Moreover, such dynamical instability implies that the harmonic lattice dynamics at 0 K cannot accurately capture the lattice vibrational properties of the constituent atoms at the elevated temperature, and consequently, anharmonic lattice dynamics is necessary to reasonably describe the lattice dynamical stability and vibrational properties at finite temperature for the monoclinic $\text{Cs}_4\text{CuSb}_2\text{Cl}_{12}$.

To this end, we then performed self-consistent phonon (SCP)



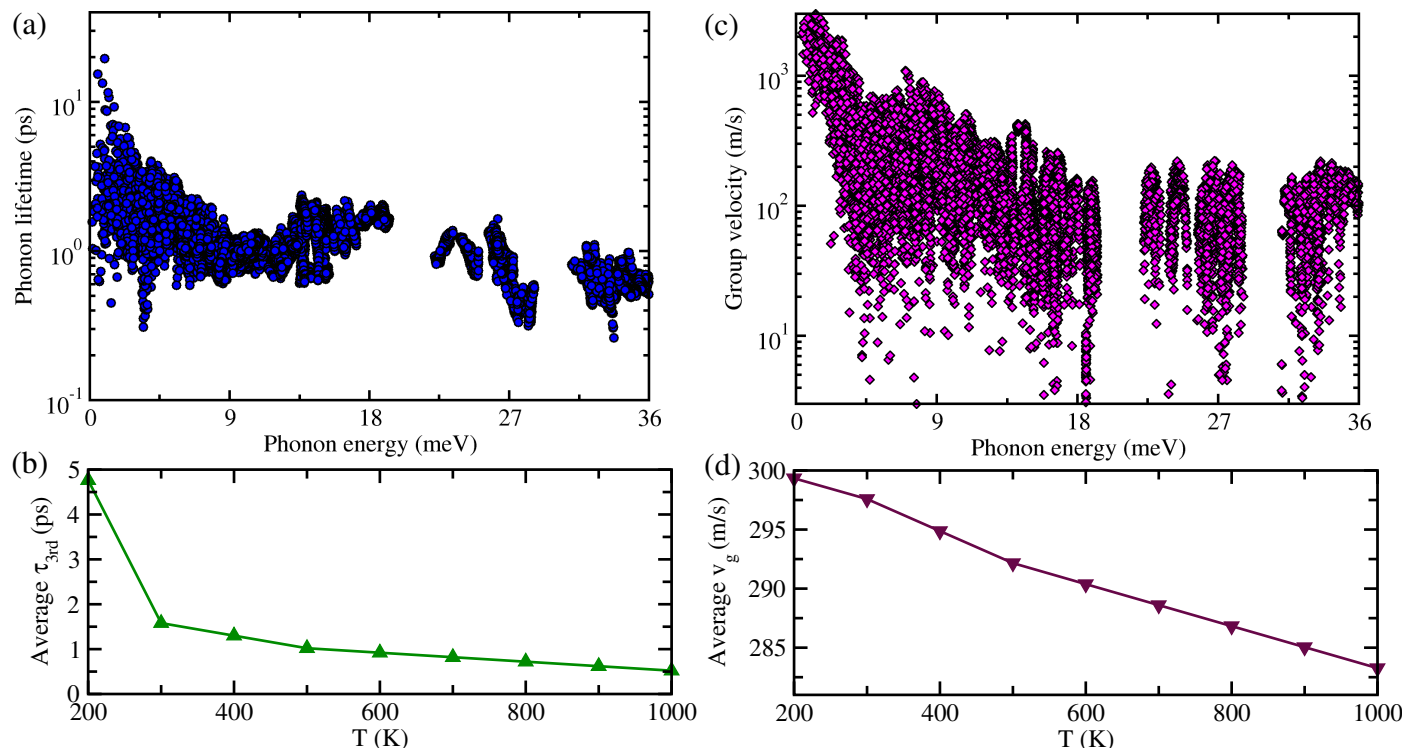


Fig. 4 (a) Phonon lifetime τ_{3rd} and (c) phonon group velocity v_g calculated as functions of phonon energy at 300 K, and (b) and (d) average τ_{3rd} and v_g calculated as functions of temperature within the self-consistent phonon approach for the quadruple halide perovskite $\text{Cs}_4\text{CuSb}_2\text{Cl}_{12}$ with the monoclinic phase of $C2/m$ space group.

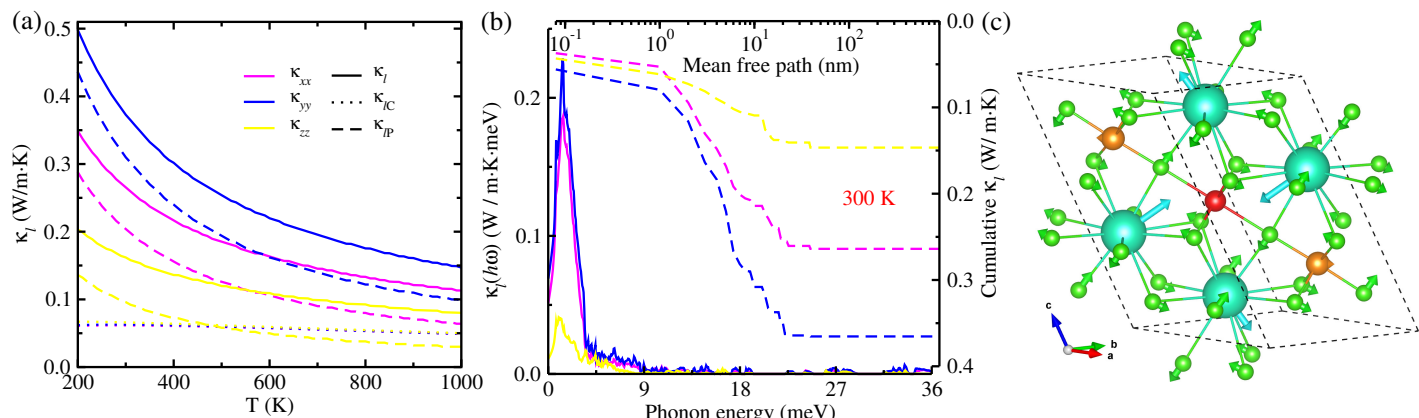


Fig. 5 (a) Lattice thermal conductivity κ_l (solid) with Peierls's contribution κ_{lP} (dashed) and coherent contribution κ_{lC} (dotted) as functions of temperature T , (b) thermal conductivity spectra $\kappa_l(h\omega)$ as a function of phonon energy (solid) and cumulative κ_l as a function of mean free path (dashed) calculated on top of the SCP eigenvalues at 300 K, and (c) ball-and-stick view of rattling vibrations of constituent atoms corresponding to the lowest optical phonon mode at the Γ point of the phonon BZ for the quadruple halide perovskite $\text{Cs}_4\text{CuSb}_2\text{Cl}_{12}$ with monoclinic phase of $C2/m$ space group. The cyan, red, orange and green balls (arrows) represent the Cs, Cu, Sb and Cl atoms (atomic vibration), respectively.

calculations to compute the phonon eigenvalues by considering the anharmonic effects at finite temperatures. Fig. 2(a) also shows the anharmonic phonon dispersion curves (magenta) calculated at 300 K for the monoclinic $\text{Cs}_4\text{CuSb}_2\text{Cl}_{12}$. In comparison with the harmonic phonon dispersion curves (brown) at 0 K, the soft phonon modes with the imaginary eigenvalues were renormalized to become real energies at 300 K. This clearly demonstrates that the monoclinic phase of the quadruple halide per-

ovskite $\text{Cs}_4\text{CuSb}_2\text{Cl}_{12}$ become dynamically stable at finite temperatures. When the temperature increases from 0 K to 300 K, the acoustic as well as optical phonon modes are noticeably renormalized across the whole range of the phonon BZ, demonstrating the strong lattice anharmonicity. Importantly, the lowest optical phonon modes are present at about 4.5 meV in the acoustic region at the phonon BZ center, indicating the strong coupling between the heat-carrying acoustic and low-energy op-

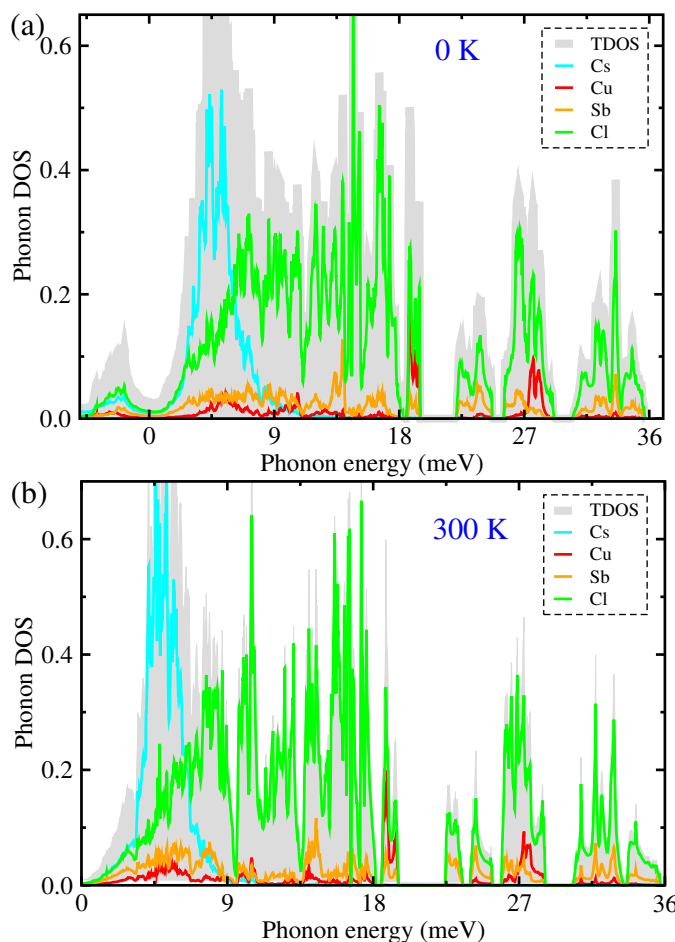


Fig. 3 Atom-resolved phonon density of states (DOS) calculated at (a) 0 and (b) 300 K by the self-consistent phonon (SCP) theory for the quadruple halide perovskite $\text{Cs}_4\text{CuSb}_2\text{Cl}_{12}$ with monoclinic phase of $\text{C}2/\text{m}$ space group.

tical modes. In the previous studies^{65,66}, it was confirmed that the low-energy optical phonons coupled with the acoustic modes play roles as strong vibrational rattlers, severely scattering heat-carrying acoustic phonons. Moreover, the phonon DOS at 300 K (Fig. 3(b)) was found to have the Cs-related phonon modes peaked around the 5 meV in the acoustic phonon and low-energy optical phonon region, which are mostly attributed to the rattling vibrations of Cs atoms. In Fig. 5(c), we intuitively show the atomic vibrations corresponding to the lowest-energy optical phonon mode at the Γ point. As can be seen, the Cs atoms have the largest amplitude among the constituent atoms, regarding as a strong atomic rattler. It can be inferred that the rattling vibrations of the Cs atoms strongly scatter the heat-carrying acoustic and low-energy optical phonons, accordingly decreasing the lattice thermal conductivity in the monoclinic $\text{Cs}_4\text{CuSb}_2\text{Cl}_{12}$. On the other hand, upon increasing temperature, the SCP dispersions broaden towards the higher phonon energy region due to the stronger thermal vibrations of the constituent atoms (see Fig. S6 in the ESI†).

3.4 Lattice transport properties

At the final stage, with the use of the SCP dispersions and DOS, and third-order interatomic force constants, we estimated the lattice transport properties such as phonon lifetime $\tau_{3\text{rd}}$, phonon group velocity v_g and lattice thermal conductivity κ_l for the monoclinic $\text{Cs}_4\text{CuSb}_2\text{Cl}_{12}$. Fig. 4(a) and (c) respectively display the calculated $\tau_{3\text{rd}}$ and v_g at 300 K as functions of phonon energy. It was found that the values of $\tau_{3\text{rd}}$ are extremely low (<20 ps) which is one order of magnitude smaller than the $\tau_{3\text{rd}}$ of the conventional thermoelectric materials, whereas the v_g is lower than ~ 2000 m/s in the whole range of phonon energy. Such low v_g at the Γ point is in reasonable agreement with the average sound velocity of 1469.98 m/s assessed by the elastic constant calculations. In particular, we note that the rapid decrement of $\tau_{3\text{rd}}$ and v_g according to the increment of phonon energy from 0 meV to 9 meV is attributed to the strong phonon scattering caused by the rattling vibrations of the Cs atoms, as confirmed above. Such small v_g and suppressed $\tau_{3\text{rd}}$ suggest that the monoclinic $\text{Cs}_4\text{CuSb}_2\text{Cl}_{12}$ can lead to extremely low lattice thermal conductivity. On the other hand, the average $\tau_{3\text{rd}}$ and v_g slowly decrease when increasing temperature because the phonon scattering intensity becomes strong according to the increment of temperature as shown in Fig. 4(b) and (d).

By using the calculated $\tau_{3\text{rd}}$ and v_g , we eventually assessed the Peierls's contribution κ_{lP} to the lattice thermal conductivity κ_l following the formula $\kappa_{lP} = \Sigma C_V \cdot v_g^2 \cdot \tau_{3\text{rd}}$, where C_V , $\tau_{3\text{rd}}$ and v_g are the heat capacity, phonon lifetime and group velocity, respectively. As shown in Fig. S4 in the ESI†, the calculated C_V increases rapidly when temperature goes from 0 K to 400 K and after that reaches a plateau, following the general tendency of a solid crystal. Fig. 5(a) shows the Peierls's contribution κ_{lP} (dashed), the coherent contribution κ_{lC} and total κ_l (solid) calculated along the x -, y - and z -axis for $\text{Cs}_4\text{CuSb}_2\text{Cl}_{12}$. It was observed that the κ_l is strongly anisotropic ($\kappa_{l,yy} > \kappa_{l,xx} > \kappa_{l,zz}$), i.e., the different values along the different axis. In the x - and y -axis, the κ_{lP} is dominant in comparison with the κ_{lC} over the whole range of temperature, while in the z -axis, the two contributions to the κ_l are comparing with each other. With reference to the magnitude of lattice thermal conductivity, the κ_l was estimated to be 0.27, 0.36 and 0.14 W/m·K at 300 K along the x -, y - and z -axis, respectively, which are comparable to 0.48 W/m·K of conventional thermoelectric material SnSe⁶⁴ and even one order of magnitude smaller than 6.96 W/m·K of GeTe⁶⁷. Meanwhile, it should be noted that the κ_l computed by iteratively solving the BTE is slightly overestimated in comparison with the none-iteratively calculated one (see Fig. S7, ESI†). Such extremely low κ_l makes suggestion that the monoclinic $\text{Cs}_4\text{CuSb}_2\text{Cl}_{12}$ can be very promising for the application of thermoelectric material.

We then considered the temperature dependence of the κ_l averaged in the x -, y - and z -axis, finding the relation of $\kappa_l \propto T^{-0.72}$ for the monoclinic $\text{Cs}_4\text{CuSb}_2\text{Cl}_{12}$ (see Fig. S5 in the ESI†). Such a large deviation from the $\kappa_l \propto T^{-1}$ tendency again confirms the strong lattice anharmonicity of $\text{Cs}_4\text{CuSb}_2\text{Cl}_{12}$. To establish deep insight into the lattice transport properties, we computed the lattice thermal conductivity spectra $\kappa_l(\hbar\omega)$ as a function of



phonon energy and cumulative thermal conductivity as a function of mean free path (MFP) at 300 K within the SCP approach. As shown in Fig. 5(b) (solid), the spectra $\kappa_l(\hbar\omega)$ is dominant in the phonon energies ranging from 0 meV to 5 meV, while is negligible in the energies ranging from 5 meV to 9 meV and high-energy region. This indicates that the acoustic phonon modes coupled with the low-energy optical modes below 5 meV have a major contribution to the κ_l , while the phonons corresponding to the optical modes over 5 meV are strongly scattered by the Cs atomic rattling vibrations, severely suppressing the κ_l for the monoclinic $\text{Cs}_4\text{CuSb}_2\text{Cl}_{12}$. Furthermore, we compared the κ_l of $\text{Cs}_4\text{CuSb}_2\text{Cl}_{12}$ with Cu^{2+} atoms and CaCuP with Cu^{1+} atoms to gain a deeper understanding of the lattice thermal transport properties. The $\text{Cs}_4\text{CuSb}_2\text{Cl}_{12}$ exhibits one order of magnitude smaller κ_l than the CaCuP ⁶⁸ due to the strong rattling vibrations of Cs atoms. In addition, the cumulative κ_l (dashed) in Fig. 5(b) is saturated at the MFP of about 40 nm, finding that the dominant heat-carrying phonons have MFP ranging from 2 nm to 20 nm. The MFPs are significantly suppressed and much less than phonon wavelength or inter-atomic spacing, violating the Ioffe-Regel limit⁶⁹. This violation supports the strong lattice anharmonicity and ultralow lattice thermal conductivity. Moreover, we note that the κ_l can be decreased by half for the nano-structure $\text{Cs}_4\text{CuSb}_2\text{Cl}_{12}$ with a size less than 10 nm.

4 Conclusions

In this work, we have systematically investigated structural, mechanical, lattice dynamics and thermal transport properties of quadruple halide perovskite $\text{Cs}_4\text{CuSb}_2\text{Cl}_{12}$ in monoclinic phase using state-of-the-art first-principles methods. Structural optimization calculations revealed that PBEsol-optimized lattice constants and bond lengths are in good agreement with available experimental data. In particular, scrutiny of crystalline structure turned out that Cs atoms are located inside over-sized cub-octahedral cage-like structure CsCl_{12} , while Cu (Sb) atoms are tightly filled into octahedral $\text{Cu}(\text{Sb})\text{Cl}_6$ cages, expecting a role of atomic rattler for the Cs atoms. We then performed anharmonic lattice dynamics calculations at finite temperature based on self-consistent phonon theory, demonstrating that the monoclinic phase of $\text{Cs}_4\text{CuSb}_2\text{Cl}_{12}$ is dynamically stable at elevated temperature. Moreover, we found that the Cs atomic rattlers stimulate lattice anharmonicity and severely scatter heat-carrying acoustic and low-energy optical phonons, consequently leading to small phonon group velocity and extremely short phonon lifetime. At the end, we calculated temperature-dependent lattice thermal conductivity of the monoclinic $\text{Cs}_4\text{CuSb}_2\text{Cl}_{12}$ using unified theory of thermal transport for both crystals and glasses, demonstrating an extremely low lattice thermal conductivity of 0.27, 0.36 and 0.14 W/m·K at 300 K along the x -, y - and z -axis. Moreover, it was found that nano-structuring can further suppress the κ_l by half for $\text{Cs}_4\text{CuSb}_2\text{Cl}_{12}$. Strong lattice anharmonicity was again confirmed from Grüneisen parameter calculation and temperature dependence of lattice thermal conductivity, *i.e.*, $\kappa_l \propto T^{-0.72}$. In addition, elastic constant calculation illustrated that the monoclinic $\text{Cs}_4\text{CuSb}_2\text{Cl}_{12}$ is mechanically stable with a brittle nature. Our work highlights atomic insights into lattice dynamics and

thermal transport properties of the quadruple halide perovskite $\text{Cs}_4\text{CuSb}_2\text{Cl}_{12}$ with monoclinic phase.

Data availability

The data that support the findings of this study are available from the corresponding author upon reasonable request.

Author contribution

Un-Sok Pak developed the original project, performed the calculations and drafted the first manuscript. Dok-Song Che Gal and Song-Myong Jang assisted with the DFT calculations and the post-processing of calculation results, and contributed to useful discussions. Un-Sok Pak and Un-Gi Jong supervised the work. All authors reviewed the manuscript.

Conflicts of interest

There are no conflicts to declare.

Acknowledgments

This work made use of the High-Performance Computing Service via our membership of the Computing Center in Kim Chaek University of Technology. The authors are extremely grateful to Prof. S.-I. Jo, Song-Gun Kim and Gyong-Sok Kim for the useful discussion and provision of scripts allowing the calculation.

References

- 1 A. Kojima, K. Teshima, Y. Shirai and T. Miyasaka, *J. Am. Chem. Soc.*, 2009, **131**, 6050–6051.
- 2 G. Niu, W. Li, J. Li, X. Liang and L. Wang, *RSC Adv.*, 2017, **7**, 17473–17479.
- 3 W. Xu, Q. Hu, S. Bai, C. Bao, Y. Miao, Z. Yuan, T. Borzda, A. J. Barker and E. Tyukalova, *Nat. Photonics*, 2019, **13**, 418–424.
- 4 K. Lin, J. Xing, L. N. Quan, F. P. G. de Arquer, X. Gong, J. Lu, L. Xie, W. Zhao and D. Zhang, *Nature*, 2018, **562**, 245–248.
- 5 National Renewable Laboratory, *Best Research-Cell Efficiency Chart*, Accessed 2019-07-12, <https://www.nrel.gov/pv/cell-efficiency.html>.
- 6 W. J. Yin, T. Shi and Y. Yan, *Adv. Mater.*, 2014, **26**, 4653–4658.
- 7 Z. Xiao, W. Meng, J. Wang, D. B. Mitzi and Y. Yan, *Mater. Horiz.*, 2017, **4**, 206–216.
- 8 Z. Xiao and Y. Yan, *Adv. Energy Mater.*, 2017, **7**, 1701136.
- 9 R. A. Evarestov, E. A. Kotomin, A. Senocrate, R. K. Kremer and J. Maier, *Phys. Chem. Chem. Phys.*, 2020, **22**, 3914–3920.
- 10 Y.-X. Zhang, H.-Y. Wang, Z.-Y. Zhang, Y. Zhang, C. Sun, Y.-Y. Yue, L. Wang, Q.-D. Chen and H.-B. Sun, *Phys. Chem. Chem. Phys.*, 2017, **19**, 1920–1926.
- 11 F. Dybala, R. Kudrawiec, M. P. Polak, A. P. Herman, A. Sieradzki and M. Maczka, *Mater. Adv.*, 2025, **6**, 569–579.
- 12 T. Krishnamoorthy, H. Ding, C. Yan, W. L. Leong, T. Baikie, Z. Zhang, M. Sherburne, S. Li, M. Asta, N. Mathews and S. G. Mhaisalkar, *J. Mater. Chem. A*, 2015, **3**, 23829–23832.
- 13 X. Zhang, Y. Ma, X. Chen, X. Li, W. Zhou, N. A. N. Ouedraogo, Y. Shirai, Y. Zhang and H. Yan, *RSC Adv.*, 2021, **11**, 33637–33645.



14 W. Chen, X. Xin, Z. Zang, X. Tang, C. Li, W. Hu, M. Zhou and J. Du, *Phys. Chem. Chem. Phys.*, 2017, **19**, 115–120.

15 Y. Takahashi, R. Obara, Z. Z. Lin, T. Naito, T. Inabe, S. Ishibashi and K. Terakura, *Dalton Trans.*, 2011, **40**, 5563–5568.

16 Y. Han, X. Cheng and B.-B. Cui, *Mater. Adv.*, 2023, **4**, 355–373.

17 N. K. Noel, S. D. Stranks, A. Abate, C. Wehrenfennig, S. Guarnera, A.-A. Haghaghirad, A. Sadhanala, G. E. Eperon, S. K. Pathak and M. B. Johnston, *Energy Environ. Sci.*, 2014, **7**, 3061–3068.

18 A. E. Shalan, *Mater. Adv.*, 2021, **1**, 292–309.

19 X. Jiang, Z. Zang, Y. Zhou, H. Li, Q. Wei and Z. Ning, *Acc. Mater. Res.*, 2021, **2**, 210–219.

20 T. L. Hodgkins, C. N. Savory, K. K. Bass, B. L. Seckman, D. O. Scanlon, P. I. Djurovich, M. E. Thompson and B. C. Melot, *Chem. Commun.*, 2019, **55**, 3164–3167.

21 S. Chander and S. K. Tripathi, *Mater. Adv.*, 2022, **3**, 7198–7211.

22 K. Mahmood, S. Sarwar and M. T. Mehran, *RSC Adv.*, 2017, **7**, 17044–17062.

23 G. Volonakis, M. R. Filip, A. A. Haghaghirad, N. Sakai, B. Wenger, H. J. Snaith and F. Giustino, *J. Phys. Chem. Lett.*, 2016, **7**, 1254–1259.

24 M. R. Filip, S. Hillman, A. A. Haghaghirad, H. J. Snaith and F. Giustino, *J. Phys. Chem. Lett.*, 2016, **7**, 2579–2585.

25 X.-G. Zhao, D. Yang, J.-C. Ren, Y. Sun, Z. Xiao and L. Zhang, *Joule*, 2018, **2**, 1662–1673.

26 T. T. Tran, J. R. Panella, J. R. Chamorro, J. R. Morey and T. M. McQueen, *Mater. Horiz.*, 2017, **4**, 688–693.

27 E. T. McClure, M. R. Ball, W. Windl and P. M. Woodward, *Chem. Mater.*, 2016, **28**, 1348–1354.

28 F. Giustino and H. J. Snaith, *ACS Energy Lett.*, 2016, **1**, 1233–1240.

29 M. K. Jana, S. M. Janke, D. J. Dirkes, S. Dovletgeldi, C. Liu, X. Qin, K. Gundogdu, W. You and V. Blum, *J. Am. Chem. Soc.*, 2019, **141**, 7955–7964.

30 B. A. Connor, F. Leppert, M. D. Smith, J. B. Neaton and H. I. Karunadasa, *J. Am. Chem. Soc.*, 2018, **140**, 5235–5240.

31 E. Greul, M. L. Petrus, A. Binek, P. Docampo and T. Bein, *J. Mater. Chem. A*, 2017, **5**, 19972–19981.

32 Y. P. Lin, S. Hu, B. Xia, K. Q. Fan, L. K. Gong, J. T. Kong, X. Y. Huang, Z. Xiao and K. Z. Du, *J. Phys. Chem. Lett.*, 2019, **10**, 5219–5225.

33 B. Vargas, R. Torres-Cadena, J. Rodriguez-Hernandez, M. Gembicky, H. Xie, J. Jimenez-Mier, Y.-S. Liu, E. Menendez-Proupin, K. R. Dunbar, N. Lopez, P. Olalde-Velasco and D. Solis-Ibarra, *Chem. Mater.*, 2018, **30**, 5315–5321.

34 B. Vargas, R. Torres-Cadena, D. T. Reyes-Castillo, J. Rodriguez-Hernandez, M. Gembicky, E. Menendez-Proupin and D. Solis-Ibarra, *Chem. Mater.*, 2019, **32**, 424–429.

35 J. Xu, J.-B. Liu, J. Wang, B.-X. Liu and B. Huang, *Adv. Funct. Mater.*, 2018, **28**, 1800332–1800339.

36 X. D. Wang, N. H. Miao, J. F. Liao, W. Q. Li, Y. Xie, J. Chen, Z. M. Sun, H. Y. Chen and D. B. Kuang, *Nanoscale*, 2019, **11**, 5180–5187.

37 N. Singhal, R. Chakraborty, P. Ghosh and A. Nag, *Chem. Asian J.*, 2018, **13**, 2085–2092.

38 B. Vargas, E. Ramos, E. Perez-Gutierrez, J. C. Alonso and D. Solis-Ibarra, *J. Am. Chem. Soc.*, 2017, **139**, 9116–9119.

39 T. Cai, W. Shi, S. Hwang, K. Kobbekaduwa, Y. Nagaoka, H. Yang, K. Hills-Kimball, H. Zhu, J. Wang, Z. Wang, Y. Liu, D. Su, J. Gao and O. Chen, *J. Am. Chem. Soc.*, 2020, **142**, 11927–11936.

40 H. Karmaker, A. Siddique, B. K. Das and M. N. Islam, *Results in Engineering*, 2024, **22**, 102106–102127.

41 O. Delaire, R. Osborn, S. Rosenkranz, M. G. Kanatzidis, D.-Y. Chung, Z. Xu, G. Xu, D. L. Abernathy, D. M. Pajerowski, M. J. Krogstad, X. He and T. Lanigan-Atkins, *Nat. Mater.*, 2021, **20**, 977–983.

42 O. Z. Delaire, G. Wolfgang, C. O. Naresh, G. Ehlers, D. L. Abernathy, D. Bansal, J. Ding and M. K. Gupta, *Adv. Energy Mater.*, 2022, **12**, 00596–00604.

43 G. Kresse and J. Furthmüller, *Comput. Mater. Sci.*, 1996, **6**, 15–50.

44 G. Kresse and J. Furthmüller, *Phys. Rev. B*, 1996, **54**, 11169–11186.

45 G. Kresse and D. Joubert, *Phys. Rev. B*, 1999, **59**, 1758–1775.

46 P. E. Blöchl, *Phys. Rev. B*, 1994, **50**, 17953–17979.

47 J. P. Perdew, A. Ruzsinszky, G. I. Csonka, O. A. Vydrov, G. E. Scuseria, L. A. Constantin, X. Zhou and K. Burke, *Phys. Rev. Lett.*, 2008, **100**, 136406–136412.

48 U.-G. Jong, C.-J. Yu, Y.-H. Kye, Y.-S. Kim, C.-H. Kim, and S.-G. Ri, *J. Mater. Chem. A*, 2018, **6**, 17994–18002.

49 U.-G. Jong, C.-J. Yu and Y.-H. Kye, *RSC Adv.*, 2020, **10**, 201–209.

50 C.-J. Yu, U.-S. Hwang, Y.-C. Pak, K. Rim, C. Ryu, C.-R. Mun and U.-G. Jong, *New J. Chem.*, 2020, **44**, 21218–21227.

51 T. Tadano, Y. Gohda and S. Tsuneyuki, *J. Phys.: Condens. Matter*, 2014, **26**, 225402–225413.

52 T. Tadano and S. Tsuneyuki, *Phys. Rev. B*, 2015, **92**, 054301–054311.

53 C.-J. Pak, U.-G. Jong, C.-J. Kang, Y.-S. Kim, Y.-H. Kye and C.-J. Yu, *Mater. Adv.*, 2023, **4**, 4528–4536.

54 F. Zhou, W. Nielson, Y. Xia and V. Ozolins, *Phys. Rev. Lett.*, 2014, **113**, 185501–185505.

55 M. Simoncelli, N. Marzari and F. Mauri, *Nat. Phys.*, 2019, **15**, 809–816.

56 U.-G. Jong, C.-H. Ri, C.-J. Pak, C.-H. K. S. Cottenier and C.-J. Yu, *New J. Chem.*, 2021, **45**, 21569–21576.

57 U.-G. Jong, C. Ryu, J.-M. Hwang, S.-H. Kim, I.-G. Ju and C.-J. Yu, *Chem. Commun.*, 2024, **60**, 13400–13403.

58 U.-G. Jong, S.-H. Kim, R.-W. Ham, S. Ri, R.-J. Ri and C.-J. Yu, *Appl. Phys. Lett.*, 2024, **125**, 042203–042208.

59 S. Sharma, J. K. Dewhurst and C. Ambrosch-Draxl, *Phys. Rev. B*, 2003, **67**, 165332–165341.

60 S. F. Pugh, *Philos. Mag.*, 1954, **45**, 823–843.

61 U.-G. Jong, Y.-S. Kim, C.-H. Ri, Y.-H. Kye, C.-J. Pak, S. Cottenier and C.-J. Yu, *Chem. Commun.*, 2022, **58**, 4223–4226.



62 H. Xie, S. Hao, J. Bao, T. J. Slade, G. J. Snyder, C. Wolverton and M. G. Kanatzidis, *J. Am. Chem. Soc.*, 2020, **142**, 9553–9563.

63 E. J. Skoug, J. D. Cain and D. T. Morelli, *Appl. Phys. Lett.*, 2010, **96**, 181905.

64 L. D. Zhao, S. H. Lo, Y. Zhang, H. Sun, G. Tan, C. Uher, C. Wolverton, V. P. Dravid and M. G. Kanatzidis, *Nature*, 2014, **508**, 373–377.

65 M. Christensen, A. B. Abrahamsen, N. B. Christensen, F. Juranyi, N. H. Andersen, K. Lefmann, J. Andreasson, C. R. Bahl and B. B. Iversen, *Nat. Mater.*, 2008, **7**, 811–815.

66 U.-G. Jong, C.-J. Kang, S.-Y. Kim, H.-C. Kim and C.-J. Yu, *Phys. Chem. Chem. Phys.*, 2022, **24**, 5729–5737.

67 Y. Pei, J. Lensch-Falk, E. S. Toberer, D. L. Medlin and G. J. Snyder, *Adv. Funct. Mater.*, 2011, **21**, 241–249.

68 U.-G. Jong, C. Ryu, J.-M. Hwang, S.-H. Kim, I.-G. Ju and C.-J. Yu, *Chem. Commun.*, 2024, **60**, 13400–13403.

69 A. F. Ioffe and A. R. Regel, *Progress in Semiconductors*, Heywood: London, 1960, vol. 4, pp. 237–291.



The data that support the findings of this study are available from the corresponding author upon reasonable request.